

Structural Analysis and Performance-Based Validation of a Composite Wing Spar

James B. Moore[†], and Stephen E. Cutright[‡]
NASA Langley Research Center, Hampton, VA, 23681

Electric-motor powered aircraft possess the ability to operate with efficient energy delivery, but lack the operational range of internal combustion engine powered aircraft. This range limitation requires the use of high aspect ratio, thin-chord wings to minimize aerodynamic drag losses, which results in highly loaded composite spar structures. High aspect ratio wings are required to increase mission durations for a NASA-developed experimental multi-rotor electric powered aircraft denoted as the Scalable Convergent Electric Propulsion Technology and Operations Research (SCEPTOR) or “X-57”. This paper examines the structural performance of the composite main wing spars to validate spar strength using ply-based laminate finite element methods. Geometric scaling of a main spar test-section was initially proposed for proof-testing but sacrificed stability. Ply-based structures modeling with local structural features was implemented as a risk-reduction methodology. Ply-based modeling was selected to augment the conventional “building block” approach to reduce risk, and leverage a “performance-based” approval processes encouraged in Federal Aviation Administration (FAA) design guidance. Therefore, ply-based laminate modeling of the full-scale main spar and forward spar shear-web attachments were subsequently undertaken to determine load path complexity with predicted flight loads. Ply-based modeling included stress concentrations and interlaminar behavior at interface locations that can be obscured in traditional finite element sizing models. Analysis of the wing spar laminate ply-based models compared with bearing test coupon performance was used to reduce future wing assembly proof-testing burden and facilitate performance-based flight hardware safety for the X-57 experimental aircraft.

I. Introduction

The unique wing configuration of the NASA Scalable Convergent Electric Propulsion Technology and Operations Research (SCEPTOR) or “X-57” experimental vehicle, shown in Figure 1, was designed to exploit efficiencies of wing-mounted electric motors and potentially increase efficiency by up to five times compared with a piston-powered aircraft. The new multi-rotor wing configuration for the X-57 requires a high aspect ratio wing for aerodynamic flight performance. A fifteen-percent-thick airfoil was designed to minimize drag and implement a leading-edge high-lift system without introducing additional frontal area plate drag that decreases range.¹ This wing configuration introduces complex load paths and highly stressed internal wing structure. In order to satisfy the aerodynamic performance requirements, the wing outer mold line (OML) was also designed to minimize frontal area with a thin airfoil, which required high-performance internal structures.

The X-57 aerodynamic solution for wing design is a thirty-foot span, fowler flap wing with fifteen-percent thickness. The wing is designed as a replacement for the production wing of a Tecnam P2006 aircraft. The P2006 is a light, general aviation twin-engine aircraft of approximately 3000 pounds gross vehicle weight. The X-57 wing has a fifty-percent shorter chord than the production wing of the P2006. The X-57 wing with multiple electric motors is scheduled to replace the P2006 production aircraft wing in early 2019. To meet aerodynamic performance requirements for additional lift and slow-speed handling, twelve small high-lift motors were placed along the leading edge of the wing. Two larger outboard motors, at the wing tips, are used for cruise operations. The limited section depth of the wing OML and motor placement creates high bending loads on the internal structure, which necessitates multiple spars to ensure the primary structure (critical to safety) meets strength requirements for fail-safe structures.^{2,3,4} The X-57 wing contains three main spars to carry bending, torsion and vertical loads. The main or (middle) spar bears

[†] Research Aerospace Engineer, Structural Mechanics and Concepts Branch, Mail Stop 190

[‡] Aerospace Engineer, Structural and Thermal Systems Branch, Mail Stop 431

the majority of bending loads while the forward and rear spar, which are wing to fuselage attachment locations, bears the vertical loading.

Performance-based validation of the wing design was selected to provide the basis for airworthiness approval of the X-57 wing to reduce costs and simplify the design process. This performance-based proof-test and airworthiness approval also required the use of a modified building-block process to substantiate individual structural elements. The traditional building block method, as shown in the Composite Materials Handbook,⁵ is a substantiation method that examines each structural element of an assembly beginning with small coupon tension tests and concluding with a full wing assembly proof-test.



Figure 1. SCEPTOR or X-57 electric motor powered aircraft.

In order to satisfy the structural design requirements of the building block method and reduce material requirements, a scaling optimization of the main spar finite element model (FEM) was investigated. This optimization was used to determine if scaling of the main spar was a practical element of the building block test method that would result in a less costly spar proof-test. Instabilities that were suspected to emerge in scaling optimizations also led to the use of a full-scale ply-based representation of the main and forward spars. Ply-based analysis models used for the spars provided a ply-by-ply modeling technique to ensure features with stress concentrations, like radii and rapid thickness changes (joggles) were fully represented. The building block flow chart, shown in Figure 2, depicts these validation processes that were used together for the forward spar assembly coupon FEM at full-scale that predicts full wing assembly performance.

Figure 2 shows the three methods implemented to verify critical structures strength that were used together. Method 1, on the lower left, shows the main spar stress-ratio based scaling optimization used to reduce material requirements. Due to anticipated non-linearity, two additional full-scale methods were developed concurrently. Method 2, in the left middle of Figure 2, shows a full-scale bearing test coupon that was used to evaluate displacement versus load to demonstrate required strength of the spar attachment. Method 3, on the upper left of Figure 2, employed a full-scale ply-based composite spar and a separate shear web FEM to identify stress concentrations. The shear web FEM of Method 3 also contained adjusted boundary conditions, to match the flight wing constraints, and ply-based detail features for more accurate stress predictions of the shear web attachment. Method 2 and Method 3 were then combined to compare full-scale shear web bearing test results with a detailed feature ply-based FEM coupon assembly. This combination of analysis and test methods was conducted to predict performance of the flight-wing assembly during proof-test depicted in the lower right portion of Figure 2.

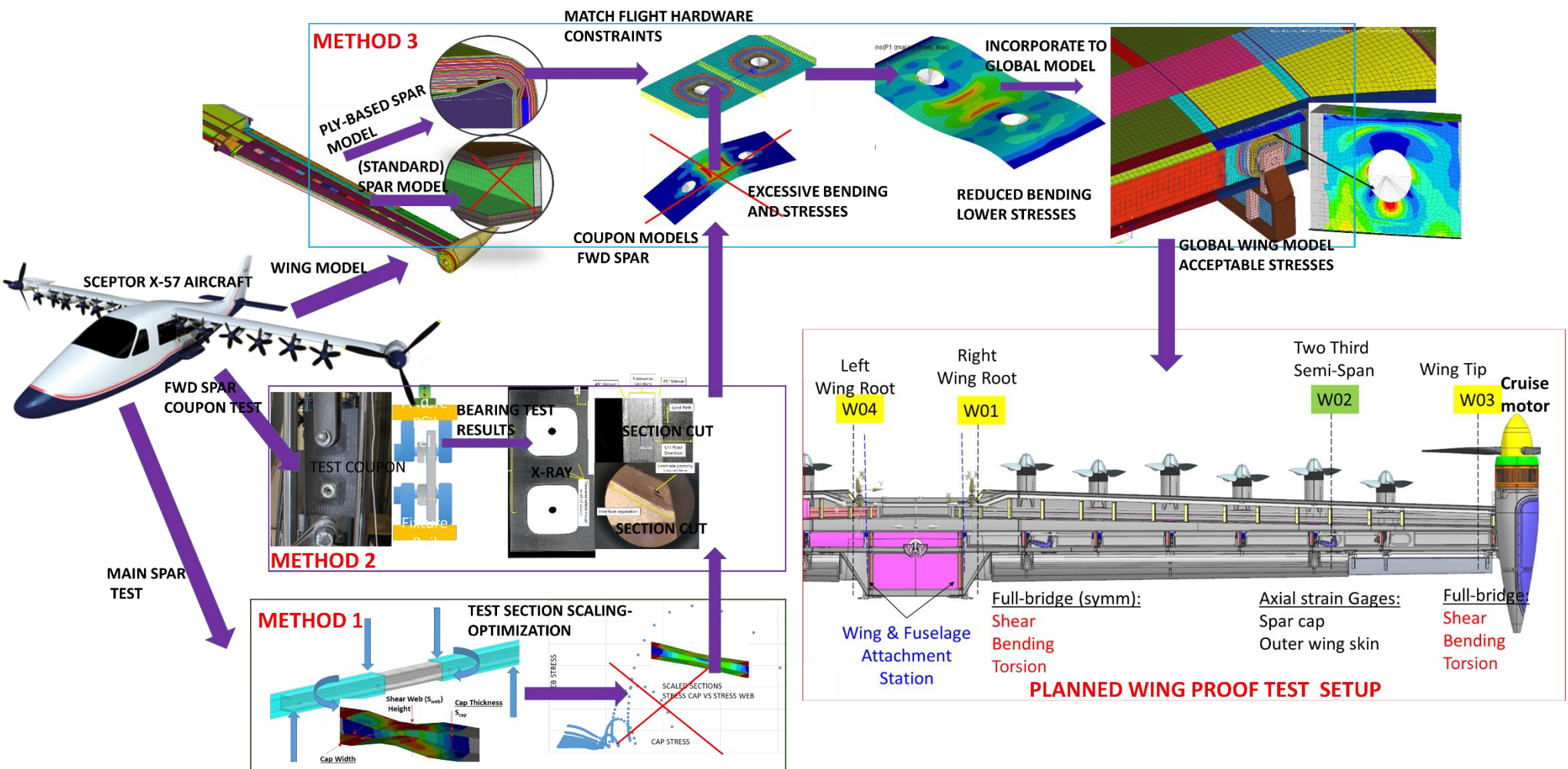


Figure 2: Modified building block methods- analysis and testing process flow

Results of the full-scale ply-based spar studies presented in this paper will be compared to test data from a planned proof-load test of the instrumented flight-wing assembly at NASA Armstrong Flight Research Center (AFRC) in mid-2019. For the main spar, a stress-ratio based scaling optimization was used to evaluate feasibility of a four point bending spar test center section, to form a part of the building block process, and is introduced in Section II. This stress-based optimization leveraged a spar scaling method that evaluated the potential for nonlinear behavior and instability with changing ply thickness and height. Section III introduces a ply-based FEM method to represent detail features with stress concentrations, that was utilized in the building block for performance-based validation of the forward wing spars. Section IV presents the forward spar coupon test data and analysis validation using a ply-based model that will be extended to validation of main wing proof-testing at a future date. Conclusions and future work for this research task is presented in Section V.

II. Geometric Scaling and Structural Similitude of Finite Element Models

A parametric scaled FEM of the main wing spar test-section was created from the full-span main wing spar FEM to determine the effects to load path and variable geometry. This was done with the goal of simplifying proof-test setup for validating manufactured component strength. To create a simplified proof-test, we explored scaling of the spar test-section, using a “standard” PCOMP element⁶ model as a baseline. This spar test-section was designed for use in a four-point bending test shown in Figure 3. This model was used to proportionally scale spar features, such as the spar cap height and width, and ply thickness (using HyperStudy⁷) at the spar test section to examine the sensitivity of combined stresses to these permutations.

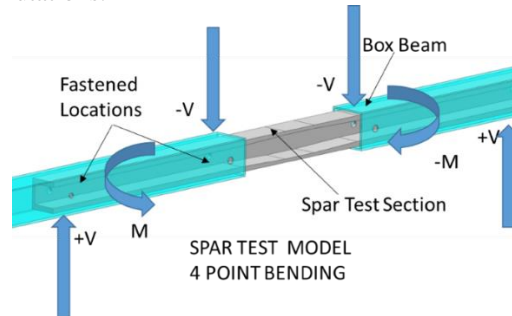


Figure 3. Equivalent load four-point bending proof-test concept for scaled composite spar section.

The scaled section of the main spar centerline ranged from uniform ratios of spar and shear-web thickness to minimum gage stringer-like designs commonly found in aircraft structures.⁸ As an alternative to simple geometric scaling, distortion-based similarity models were also used to guide the selection of ply thickness rather than ply count to reduce low ply-count instabilities and scaling uncertainty.^{9,10,11} The FEM of the test-section was simultaneously scaled for geometry and ply thickness in the optimization study. This provided insight into structural load paths by examining stress-ratios on critical features like adjacent spar caps and shear-webs.

Composite structural models can demonstrate significant load path discontinuity for joined sections (i.e., shear-webs, spar caps and spar attachment hard-points) when features like corner radii are not represented in the scaled approach with the standard model. Composite structures can also demonstrate a lack of damage tolerance resistance and anisotropic behavior for geometric permutations. This can occur if the scaled design trends towards a minimum gage equivalent of two or three plies total thickness.⁸ Therefore, the main spar FEM, a critical structural element, was selected for the baseline model scaling investigation. The main spar FEM was scaled geometrically and with ply thickness simultaneously to vary centerline test-section geometry and spar features total thickness. This approach aided in characterization of load path behavior and modeling validation of the main spar and a forward spar wing attachment bearing test discussed in Section III.

A. Computational Approach for Test Section Scaling and Optimization

An automated analysis approach, implemented in HyperStudy, was used to create a parametric stress-based optimization that varied section height and thickness of the standard main spar model. A composite FEM of the main spar was created with 21,918 elements and 274,272 degrees of freedom. The gradient-based scaling optimization maximized stress-ratios of adjacent features of the spar model. Flight loads^{12,13} obtained from the wing assembly FEM were applied to the main spar model free body diagram (FBD). The scaled spar center section optimization, in

Figure 4, utilized stress-ratio performance objectives with buckling stability eigenvalues as one constraint. Strength performance values were obtained with variations in cap thickness, width, and ply thickness.

The objective function is based on adjacent feature stress-ratios, shown in Equations 1-3. Objective function variables, shown in Figure 4 (lower right), maximized the combined stresses of the unsupported spar cap regions with the adjacent shear-web stresses to determine load transfer effectiveness.

$$\text{Objective Function, } f(x): 0 \ll SR \leq 1, \text{ where:} \quad (1)$$

$$\text{Stress Ratio (SR): } \frac{S_{web}}{S_{cap}}, \quad S_{web, cap} = \text{Stress at webs and caps} \quad (2)$$

$$\text{Constraints: } SR \leq 1, \lambda > 1, \lambda = \text{Buckling Eigenvalue} \quad (3)$$

This method explored maximization of shear-web versus spar cap stress-ratios towards unity to encourage greater load transfer between the two but avoid trivial full-thickness (block-like) structures with artificially low stresses and higher weight penalties. Thinner and smaller height sections were anticipated to demonstrate nonlinear stress trends with the scaled section height and shear-web thickness variations. The objective function strategy forced spar feature geometries towards a localized fully stressed design (FSD) result, with higher stresses, to promote failure of an optimized test-section at the centerline location. This objective function also aimed to reduce the test-section size, which had potential to reduce hardware requirements at the expense of mesh resolution.¹⁴ Results of the parametric scaling analysis are presented next in Section II.B.

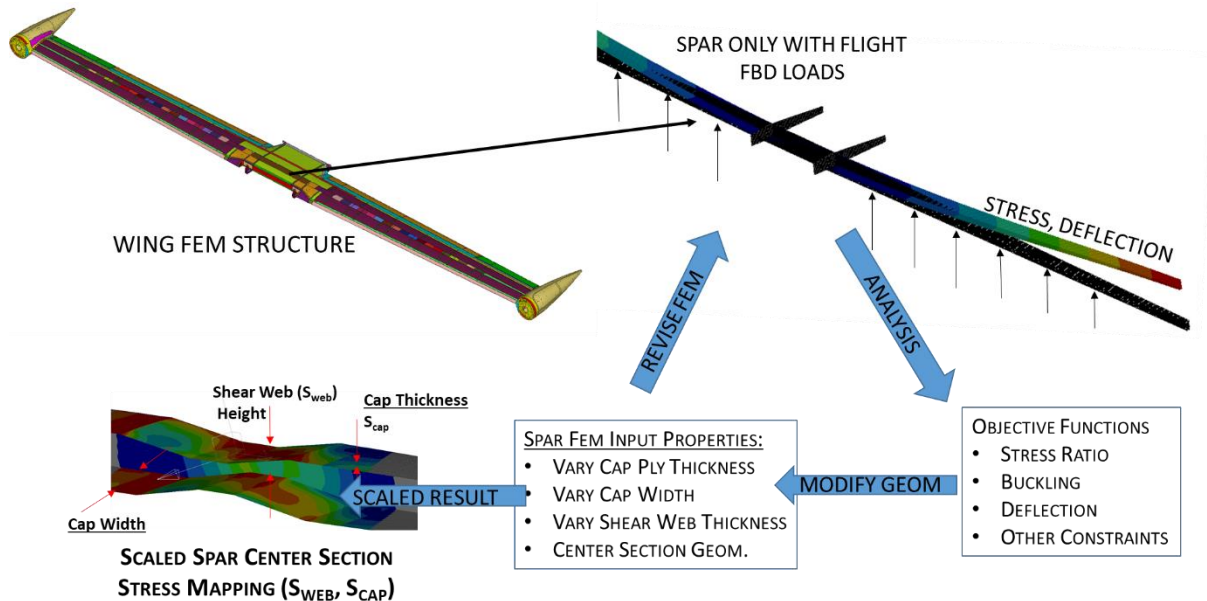


Figure 4. Automated method for main spar FEM structural scaling optimization.

B. Scaled Test Section Optimization Results

Flight loads, shown in Figure 5, were applied to this model using grid-point forces extracted from the full wing assembly FBD and contractor provided load sets.¹³ These loads were used to examine displacement, stress, and stability in the wing spar test section “neck down” (centerline) region. The neck down region is shown lower left of Figure 4, where failure would be desired during component proof-test. The shear-web height, spar cap, and ply thickness in this region were varied to promote uniform load transfer between spar features at the anticipated test-failure site. This test region was designed to evaluate the load paths and stress concentrations while maintaining buckling stability of the component.

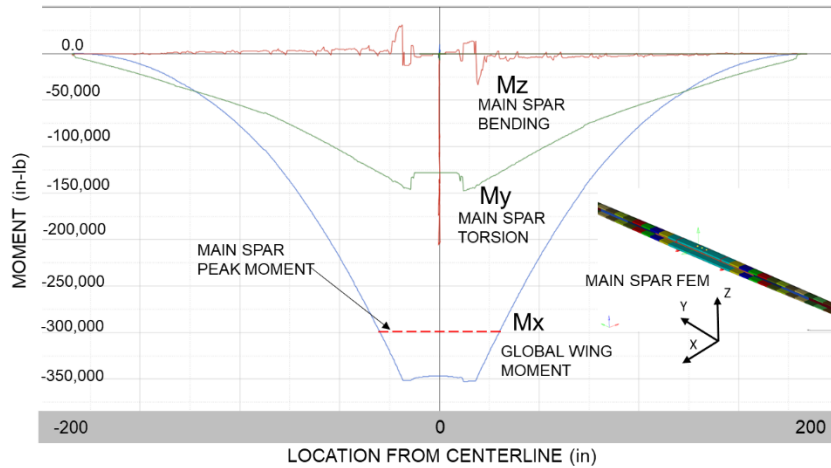


Figure 5. Spar bending and torsion moment diagram, maneuver flight load - FEM derived.

The moment plot, shown in Figure 5, indicates that the main spar absorbs a majority (over 80 percent) of the 350,000 inch-pound global wing bending moment. This is due to the high stiffness of the main spar, which is considered critical (primary) structure.

The FBD loads were applied to the main spar with four displacement constraint sets, derived from the wing assembly FEM. Constraints were applied at intercostal rib locations where the main wing attaches to the fuselage. The optimization varied the ply thickness of the caps and shear-web simultaneously using a Global Response Surface Method (GRSM) optimization.⁷ Thickness of the cap and webs were simultaneously varied in the ply sequencing from 0.02 to 0.25 inch. Geometric scaling (height and width) of the standard model was accomplished by uniformly ‘morphing’ the shell element geometry using the HyperStudy tool suite.⁷

Stress-ratios of unsupported spar cap locations compared with adjacent shear-web locations were used as inputs to the objective function. A spectrum of optimization results showed thickened spar caps stress-ratios less than one for conventional spar designs shown in the lower left of Figure 6. By contrast very thin cap FSD-like result with stress-ratios approaching one (full local load transfer) are shown on the right. More uniform FSD-like outcomes resulted in uniform stress transfer, but lower stability (eigenvalues (λ) less than 1) for thin-ply and shorter shear-web height combinations.

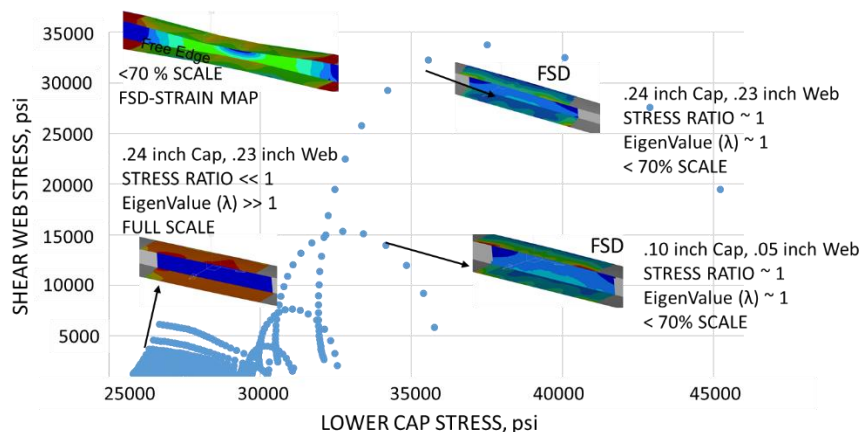


Figure 6. Stress-ratio optimization of a scaled main spar fully stressed design.

Stress-ratios approaching unity, on the right, demonstrate more uniform stress distribution throughout the part, but linearized bending load distribution through the neutral axis of the part was maintained.⁸ This FSD-like trend appeared for numerous geometries and ply thickness combinations shown in the scatter plots on Figure 6.

Nonlinear stress trends were observed in the upper caps when scaled down below 70 percent of original height. The stress map also had non-uniform chord-wise and span-wise load distribution at free edges shown in the stress plot Figure 6, upper left. As shear-web height was reduced, the spar caps gradually increased in strain loading which represented a different load path than the full-scale design. Spar cap stability was also reduced for sub-scale designs with shorter shear-web height and eigenvalues less than one. A trivial result of a full depth section and full ply-thickness with reduced shear-web loading and spar cap stress was confirmed in Figure 6 (lower left). For the cases of full web depth and maximum ply-thickness of a conventional full-scale design, the stress-ratios were very low with high buckling resistance where eigenvalues are greater than unity.

III. Composite Wing Spar Ply Based Feature Analysis and Validation

Standard models with PCOMP shell elements do not directly represent bend radii and other through-thickness features, such as ply drop-offs that create stress concentrations. Therefore, a ply-based modeling approach at full-scale was used for the main spar and forward spar primary structures to verify load path and minimize testing uncertainty. An example of the performance difference between the standard PCOMP model and the ply-based model representations in a three point bending test, is shown in the insets in Figure 7. The ply-based models parametrically represented each layer of the laminate stack ply-sheets, including drop-off regions. The main spar ply-based models represented detailed features like bend radii where spar caps mate with shear-webs. The forward spar models, however, focused on wing attachment regions that contained hard-points within the laminate. This forward spar ply-based model was then inserted to the global wing FEM to compare with the initial results of the contractor provided coarse sizing FEM results in this region.¹⁵

Displacement and stress magnitudes under flight loads were nearly equivalent between standard and ply-based models for sizing purposes, although local stress concentrations on detailed features varied significantly. This difference was evident in stress concentrations found in a generic ply-based C-spar three point bending model comparison in Figure 7. For example, stress concentrations approaching 43,000 psi (43 ksi) were prevalent in the ply-based model at corner radii and joggle regions (Figure 7b). The standard PCOMP model, under the same load, however demonstrated increased load concentration in the shear-webs of approximately 77 ksi shown in Figure 7a. Similar stress magnitudes can be found at radii corners for both standard and ply-based models for the generic C-spar section.

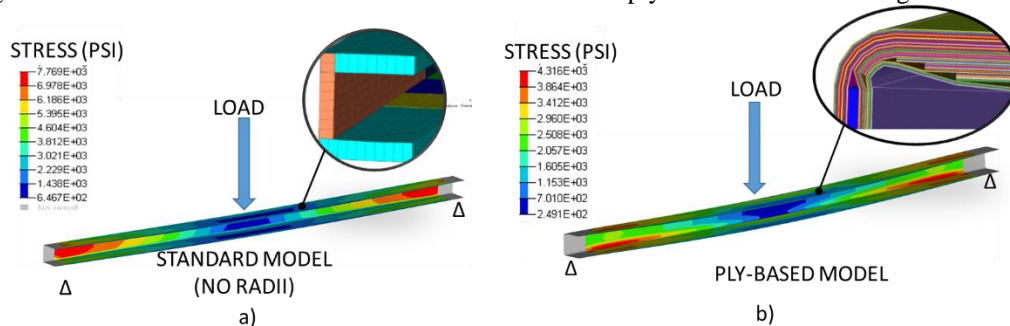


Figure 7. Three point bending of a) standard C-spar model, b) ply-based FEM C-spar model under equivalent bending loads.

The maximum principle strain angles in the C-beam experiment (Figure 8a) demonstrated a relative concentration of strain at shear-web (shown in red) regions throughout the part. This was different from ply-based model of Figure 8b, which indicates higher corner radii strain angles (and loading) by comparison. To similarly characterize shear-web behavior more closely, a test coupon for the forward spar wing attachment was modelled as shown in Figure 8c-d. The forward spar hard-point (bearing) coupon was modelled as a ply-based FEM, which contains more gentle 45-degree blended corners compared to the right-angled corners of a standard PCOMP model. This shear-web bearing coupon FEM also demonstrated different principle strain angles for the design load conditions. The ply-based model also produced a notable increase in average principle strain angle with higher strain angles indicated near the load bearing hole penetrations. This highlights the load path disparity between the standard (PCOMP) sizing model and a more detailed ply-based FEM for hardware validation.

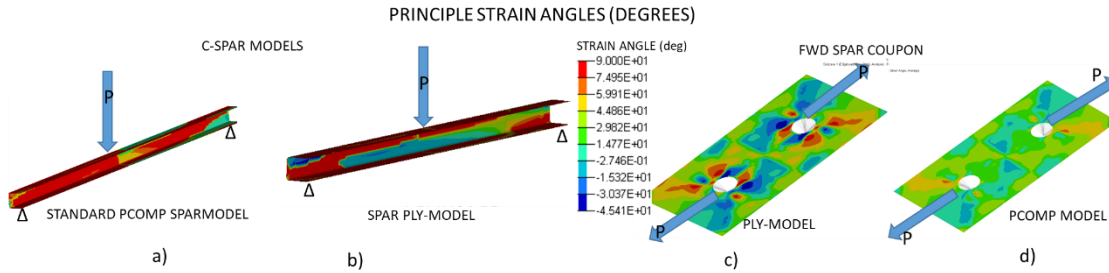


Figure 8. Principle strain angles with equivalent loads (P) of a,b) standard vs. ply-based C-spar model and c,d) ply-based vs. standard model for forward spar bearing test coupons.

For the X-57 wing assembly, the main spar stress distribution and strain margins were also notably different at detailed geometric features like radii and ply-drops as shown in Figure 9a, when comparing the standard to ply-based models. The center section of the main spar component, with aircraft maneuver loads, revealed up to a 30 percent difference in localized strains in Figure 9b between standard and ply based models features. For a required 3.42 g pull-up maneuver,¹³ the spar strains in the standard PCOMP model reached 0.0015 inch/inch strain or 1,500 microstrain (μs), whereas the ply-based model indicated 2,080 μs for the same spar features locations show in Figure 9b, a thirty percent difference. For detailed features representation, the ply-based analysis model was therefore selected for the main spar and forward spar wing attachment analysis.

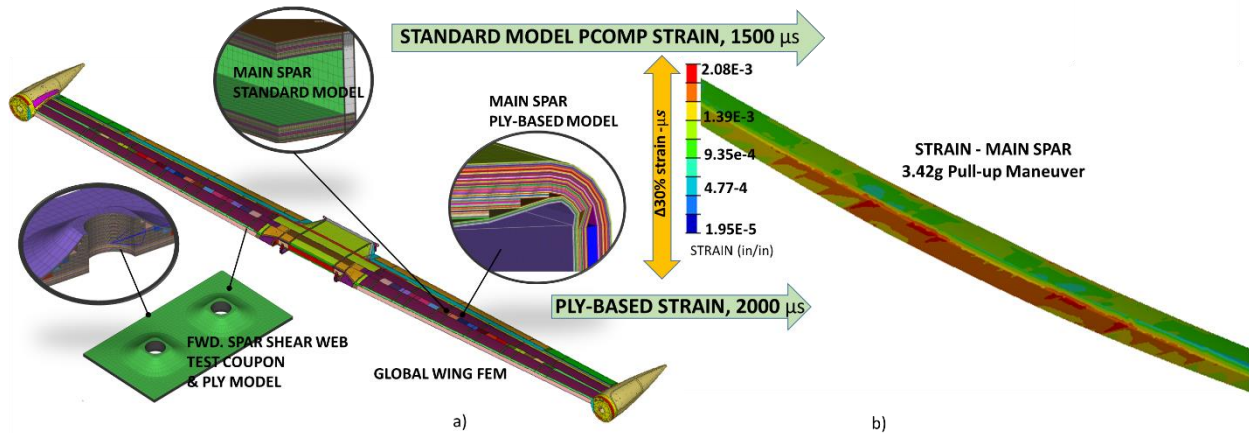


Figure 9: X-57 Wing analysis models; a) Standard wing spar model vs. ply-based composite spar FEM's, b) strain result of standard and ply-based models under maneuver loading.

This modeling technique and feature-driven load path will also be validated by a planned wing assembly proof-test in mid-2019. The wing assembly will be internally instrumented with strain gages at select locations to validate load path and strain amplitudes. Test data will be compared with FEMs, under the simulated flight load conditions, at select span-wise locations. Results of the wing assembly proof-load test will be utilized to further validate the ply-based main spar and forward spar analysis techniques. Strain gages for the wing proof-test will be located at four wing stations and consist of eight bending half-bridge, four torsion and four shear-bridges. Correlation of the performance data from proof-test with the global and more detailed ply-based models will permit a “performance-based” validation for airworthiness approval of the X-57 flight wing structures.

IV. Forward Spar Coupon Testing and FEM Validation

The X-57 wing forward attachments bear up to 80 percent of the total wing loads for all phases of flight.^{3, 13} To validate manufacturing process and component strength¹⁵ a full-scale bearing coupon section of the forward spar main wing attachment hardware was fabricated. The coupon was fabricated from a mixture of autoclaved pre-preg and wet-

lay fabric components. The assembly was tension load tested 400 percent beyond Design Limit Loads (DLL) of 3.42 g's. The DLL is the maximum design load that does not create permanent deformation of the structure. The test coupon assembly, shown in Figure 10b, consisted of two bolted lug attachments bonded to an orthotropic shear-web fabricated from carbon fiber. The test coupon was fabricated to match the shear-web portion of the forward spar fuselage attachment, but omitted spar caps found in the flight hardware. The purpose of the test coupon assembly, depicted in Figure 10c, was to demonstrate the bearing capability of the wing attachment locations.

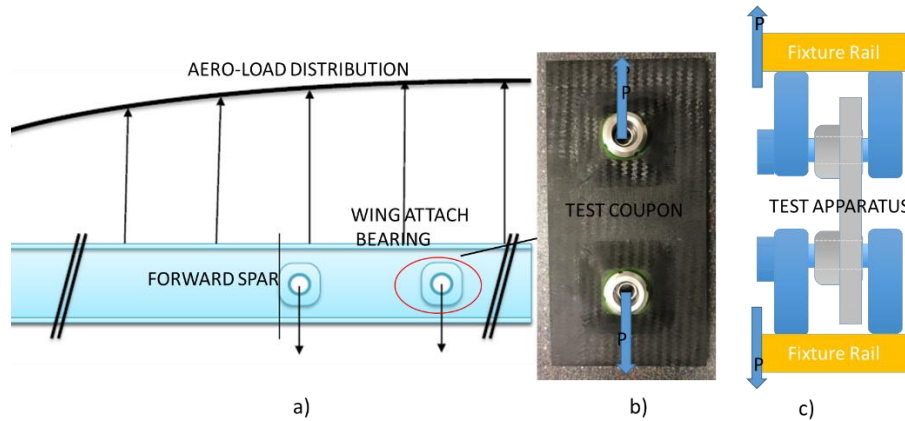


Figure 10: a) Main wing bearing locations, b) forward spar shear-web test coupon assembly, c) shear web coupon test apparatus depiction

The orthotropic laminate, Figure 10b, consisted of bidirectional (BID) fibers at the OML, whereas the inside mold line (IML) through-thickness regions contained span-wise unidirectional (UNI) fibers. UNI fibers were incorporated early in the design to improve global aeroelastic performance and strength³ described in Sections IV.A through IV.D.

A. Bearing Test Coupon Assembly Modeling

The X-57 forward wing attachment coupon FEM, Figure 11a, was a 8 inches by 15 inches carbon fiber-based test coupon assembly with 27 total plies, consisting of 14 layers of UNI cloth. The UNI cloth was sandwiched between 13 layers of BID cloth to create a stable quasi-isotropic laminate stack. The total coupon baseplate thickness was 0.27 inch and overall plate height was 0.78 inch. The test coupon also contains two phenolic (G-10) insert hard-points, Figure 11b, which were loaded in plane with bearing-eccentric tension “P” at the hard-point. The use of the interior UNI- stacked fibers in the forward spar was critical to arrest global “knife edge” aeroelastic modes that could result with the X-57 high aspect ratio wing construction and minimized structural weight.³ Load-path orthogonal UNI plies with very thick sections, however, created greater potential for matrix cracking described below.

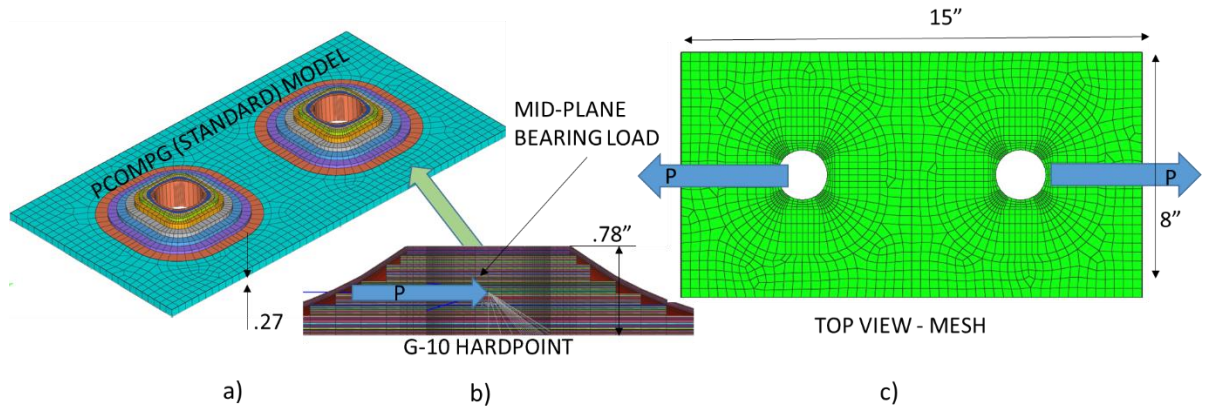


Figure 11 : a) Forward spar test coupon baseline, b) phenolic G-10 ply-based hard-point FEM, c) 2D plate mesh with test load (P)

The shear-web coupon FEM consists of 2172 ply-based composite elements and 13,848 degrees of freedom to provide a high-resolution model to observe load path behaviors. A 300 percent increase in FEM mesh density was incorporated at bearing regions to capture localized stress concentrations. The bearing load is applied at hard-point inserts (G-10 phenolic) that were also modeled using ply-based elements to ensure a consistent modeling approach. The coupon FEM did not contain bond lines between plies for the hard-point attachment to the baseplate that are used in the flight-hardware spars. This was to ensure a conservative result and avoid taking load-path credit for bonding materials that are subject to environmental process variations. Load conditions and testing results are discussed in Section IV.B-C. Section IV.D presents a performance-based analysis method using the ply-based representations for “global-local” analysis of the coupon FEM. This method was used to validate the forward wing spar bearing attachment design with displacement data obtained in the forward spar coupon assembly bearing test. The global-local method used a more detailed ply-based analysis of the global wing FEM forward spar features than originally used for coarse FEM-based structural sizing.¹⁵

B. Forward Spar Assembly FEM (Coupon) Loading Conditions:

Three separate analysis cases were reviewed in the model to predict flight hardware behavior. The first condition used a 400 percent (4x) of DLL applied to the wing lug attachment bearings. The second load condition evaluated was the modification of the coupon boundary constraints to simulate the high stiffness of the spar-caps and arrest mid-plane deflections that induced high stresses. Finally, the shear-web FEM coupon was inserted into the wing assembly FEM in Figure 12a, and subjected to 4x-DLL flight ultimate loads bearing test. Figure 12b shows the forward spar bearing test article used for building block validation.

Three load cases for the carbon fiber shear-web test coupon FEM are compared to test data in Section IV.D:

1. 4x-DLL with 20,000 pounds (20 kips) applied radially at bearing mid-plane locations.
2. Modified boundary conditions to simulate spar caps and skin constraints at 4x-DLL loading.
3. Global-Local model of half-span coupon assembly and wing assembly FEM, Figure 12a.

For all cases, maximum load application to the FEM consisted of flight maneuver loads of 4x-DLL transmitted radially to the coupon bearing mid-plane locations (Figure 12b). Residual indeterminate loads from bearing test loading were absorbed by partial-fixed boundary conditions applied to the coupon mid-span to promote FEM stability and symmetry.

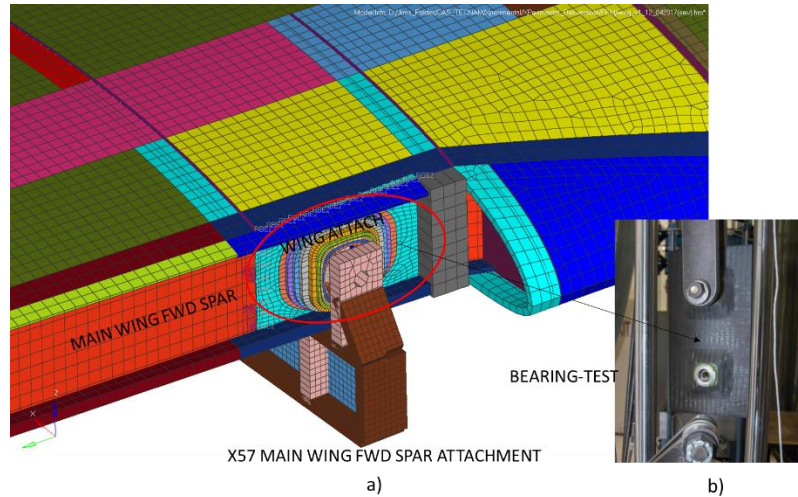


Figure 12: a) Main wing FEM global-local forward spar ply-based model, b) forward spar bearing test setup

C. Bearing Test Coupon Loading and Results:

The test coupon, as shown in Figure 12b, was installed in a fixture with proof load sets applied linearly with time at successive intervals. The first load set was applied to 5,246 pounds, or 100 percent DLL in Figure 13a, and subsequently unloaded to examine the coupon for defects and hysteresis. A linear load ramp rate of approximately 4×10^{-4} inch/second was used. The DLL loading plots to 0.040 inch relative displacement appeared uniform, with some hysteresis and observable data acquisition noise show in Figure 13a. This result cleared way for testing to the ultimate loading condition at 20 kip in Figure 13b. Ultimate loads were maintained for a minimum of 3 seconds to meet NASA flight-hardware design requirements.¹³

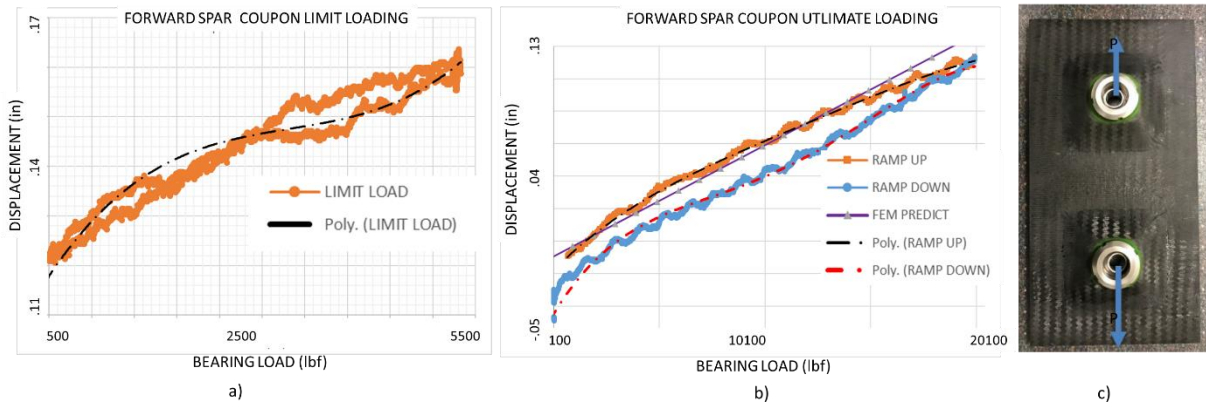


Figure 13: Design limit loading a) and b) ultimate loading of c) forward spar test coupon assembly

During ultimate load testing the specimen (Figure 13c) remained intact up to 20 kips and 0.13 inch displacement as shown in Figure 13b (orange curve), although test results revealed significant out-of-plane deflections at mid-plane. Large mid-span deflections were observed during testing and video recorded. Dashed lines in the figures (poly lines) show curve matching of data used to indicate generalized trends of the displacement curves. The solid purple line (Figure 13b) shows the ply-based FEM prediction overlaid on the test data. Displacement with load is primarily linear during DLL to ultimate testing with little hysteresis during the DLL portion of the test (Figure 13a). Significant hysteresis, indicating UNI fiber matrix failure, was encountered during ultimate loading of the coupon as indicated by the blue curve in Figure 13b. The hysteresis also indicated debonding of the hard-point at matrix interfaces, which was confirmed using X-ray inspections. X-ray examination of the coupon section-cuts after test (Figure 14) showed several matrix fracture locations on the IML of the span-wise draped UNI fibers matrix regions, but no damage to the OML BID fiber locations. Confirmation of matrix cracking and assembly debonding was

achieved by destructive evaluation with a section-cut performed on the assembly as shown in Figure 14c-d. X-ray images also indicated widespread micro-crack damage (off-white regions) to UNI fibers after ultimate loading. Closer investigation of the damage using a polished section-cut, Figure 14d, also revealed bond-line peeling at the hard-point phenolic (G-10) block insert due to eccentric (peel) loads shown below. This result drove the need for further detailed ply-based analysis of the test coupon FEM to validate performance and airworthiness of the test coupon that had different boundary constraints than expected on flight hardware. Post-testing examination of the 20 kip tension coupon under X-ray, in Figure 14a, revealed widespread resin micro-cracking of the matrix through laminate thickness primarily in the 0-degree orientation UNI fiber. Figure 14C shows matrix cracking along a section cut normal to the load application. BID cloth on the coupon exterior, however, maintained continuity without failure through ultimate loading. The BID cloth, however, did exhibit peeling at the G-10 hard-point interface locations, shown on Figure 14d, which grew with increasing loads beyond DLL, but did not affect static strength. Comparison of the test coupon results compared with a modified boundary condition coupon FEM, to address flight-wing assembly constraints which are different from test coupon, is conducted in Section IV.D.

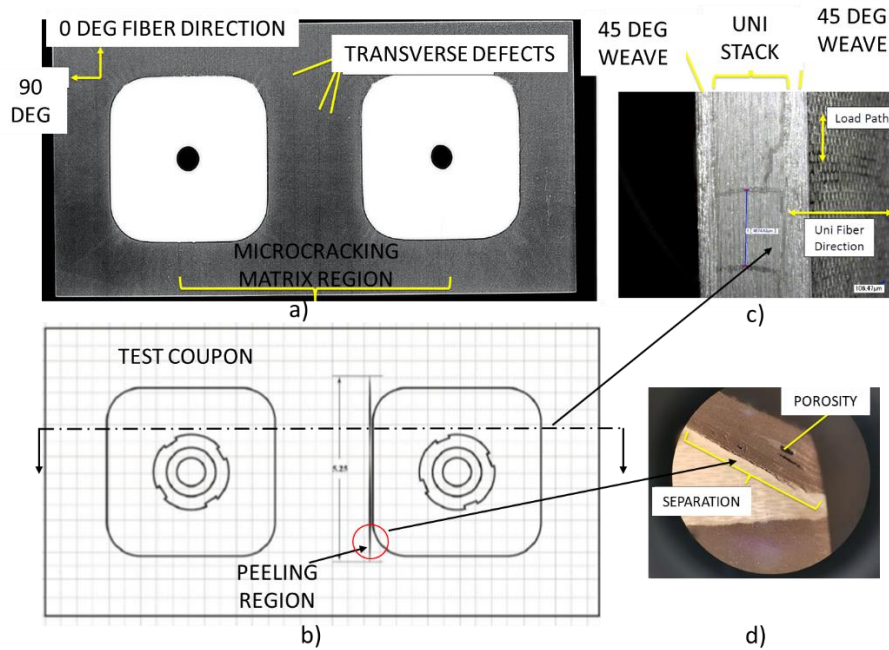


Figure 14: a) X-ray of coupon matrix micro-cracking, b) bond line peeling region of test coupon, c) UNI fiber micro-cracking after 400 percent ultimate loading, d) polished section cut of bond line peel region.

D. Analysis of Forward Spar Tension Coupon Load Cases (Verification of Observed Performance)

1. Analysis Case 1: Radial mid-plane bearing loading

To validate the DLL proof load and ultimate loading response, the ply-based FEM forward spar coupon model was also loaded to 20 kips applied radially at two mid-plane bearing locations. This loading also generated a large mid-span eccentricity in the unrestrained (through thickness) direction. Ultimate loading of the FEM resulted in out-of-plane deflections over 0.5 inch, shown in Figure 15a, observed during testing. The peak strain limits reported from the FEM at ultimate load testing was approximately +20,000 μs tension and -9,000 μs compression. This peak response occurred at phenolic hard-point and baseplate bonded locations, which showed potential for peeling failure as observed during the testing sequences and with X-ray indications. The result demonstrates the tendency of the wing attachment hard-point under eccentric loading to pull away normal from the surface, create bowing in the part, and to separate or peel from the baseplate.

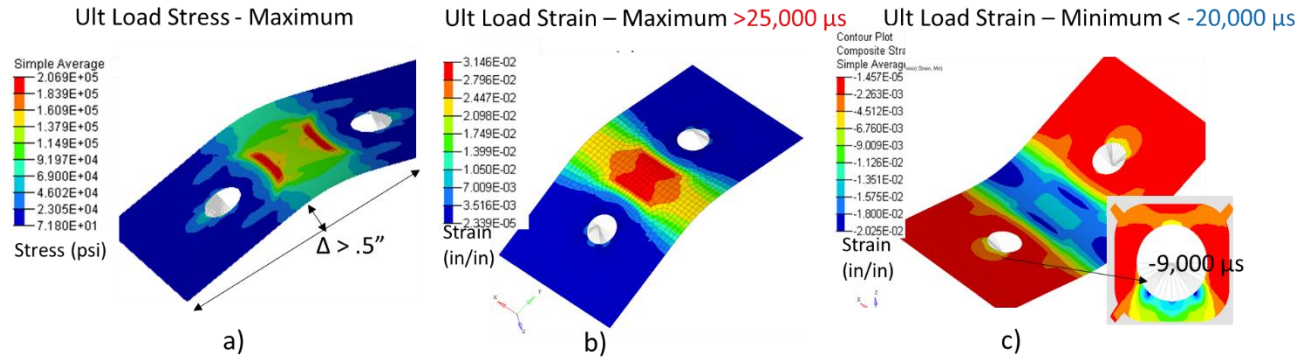


Figure 15: Bearing test coupons FEM at 20,000 pounds tension showing a) ultimate loading maximum stress and b,c) maximum and minimum ultimate loading strains.

The fiber tension strain level predicted in this hard-point-bonded location, shown in Figure 15b, is well beyond the normal working strain load for more traditional carbon-based flight hardware composites system of +6,000/-5,000 μs quasi-isotropic structure.¹⁶ This, however, demonstrated the carbon-based laminate achieved maximum published strength in static loading. Maximum loading occurred at the expense of matrix cracking, Figure 14a, for inner UNI plies aligned orthogonal to the load application direction. The performance of the outer ply BID cloth demonstrated a conservative result analytically, when compared to a more constrained (mid-span) wing attachment structure discussed in Section IV.D.3. Bearing coupon analysis also indicated potential for laminate failure at hard-point and base plate bond-line locations with elevated stress concentrations highlighted in red, Figure 15a. As previously shown in Figure 14b, bond line failures were detected in identified peel regions via X-ray and when the coupon was sectioned after ultimate testing. This examination therefore confirmed the failure prediction methodology. Compressive strains in Figure 15c indicate higher than typical values although they are within material maximum capabilities. The stress results were confirmed for margins against contractor issued reports and using coupon pull-test data obtained during material qualification, per ASTM-D3039^{16,17}. Tensile strength allowables are shown in Table 1.

Table 1: Tension test coupon material fiber and composite properties

Material	Tensile Strength (ksi)	Tensile Modulus (Msi)	Density (lb/in ³)	Weight/Length (lb/in)
IM2F4-BID*	107.9	11.9	0.064	-
IM2CF4-UNI*	263	24.48	0.064	**25.0x10 ⁻⁶
CHM12K*	57.0	13.15	0.076	-
IM7**	800 (395)	40.0 (23.8)	0.064	12.5x10 ⁻⁶
IM8**	880 (442)	45.0 (26.3)	0.064	25.0x10 ⁻⁶

* Material Allowables from Testing, Xperimental Inc – ASTM-D3039, NIAR Report NCP-RP-2017-003¹⁶
 **Maximum Material performance from Hexcel.com , (design limit values-allowables shown in parentheses), Reference Set

High stress levels encountered at bearing regions of Figure 15, which are a result of eccentric loading, remained within the material maximum performance as shown in Table I. The successful proof load ultimate test case at 4x-DLL also demonstrated a conservative design result for the flight hardware. Flight hardware contains spar cap boundary constraints that significantly reduce out-of-plane displacement and strain levels in the analysis models. The additional mid-plane and boundary constraints at edge locations are applied and described below for verification of proof-test results and full-scale predictions.

2. Analysis Case 2: Radial loading of bearing coupon and modified boundary constraints.

The bearing test coupon demonstrated large out-of-plane displacements (exceeding 0.5 inch) and strain behavior, due to the lack of mid-span boundary constraint in the as-tested configuration. This represented a conservative bearing strength evaluation of the forward spar attachment features. A modified constraint set using a FEM that more closely represents the flight hardware configuration was utilized to predict flight-wing performance. The bearing coupon FEM was modified to include mid-span constraints preventing out-of-plane displacement along a symmetric axis shown in Figure 16a (yellow constraints). Ultimate tension loads were again applied to the FEM to evaluate the stress response when compared with the unmodified FEM coupon and test results.

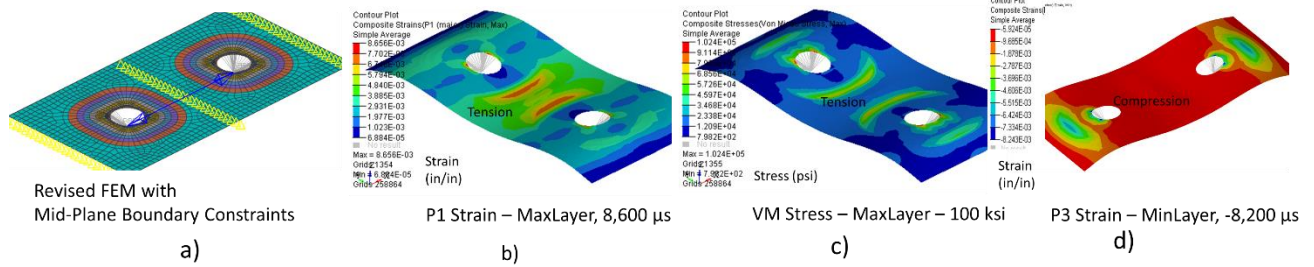


Figure 16: Tension coupon with mid-plane boundary constraints for a) finite element model representation, b,c) tensile strain/stress results of coupon, d) compression strain of coupon.

When the new FEM boundary conditions were applied, the bearing load stresses in the hard-point bonded regions of the FEM were reduced from over 20,000 μs to 8,600 μs . Combined stresses were also reduced from over 200 ksi to less than 100 ksi compared to the original model. This represented over a 57 percent reduction from the original state. Compression strains were also reduced from -21,600 μs to -8,200 μs at mid-span. This indicated the spar attachment region has sufficient margin, per Table 1 material performance limits, on the flight structures.

3. Analysis Case 3: Addition of Half-Span FEM Coupon Assembly To Global Wing Model.

Next, the global wing model insertion approach of analysis case 3 investigated the incorporation of a half-span coupon FEM into the global wing model. The FEM insertion of the coupon was to evaluate local behavior of the mesh-refined coupon in the global wing assembly model that demonstrated another element of the building block/performance based approach utilized. A half-symmetric portion of the ply-based forward spar coupon was inserted into the global wing model to transfer global wing loads to the local mesh-refined coupon FEM in Figure 17b, left. The higher mesh density of the ply-based model for the coupon was used to examine the localized behavior of the higher mesh density coupon FEM. This global wing model is subjected to a span-wise load distribution as shown in Figure 10, and additional adjacent structural stiffness-constraints from the full assembly flight-wing model containing spar caps and wing skins.

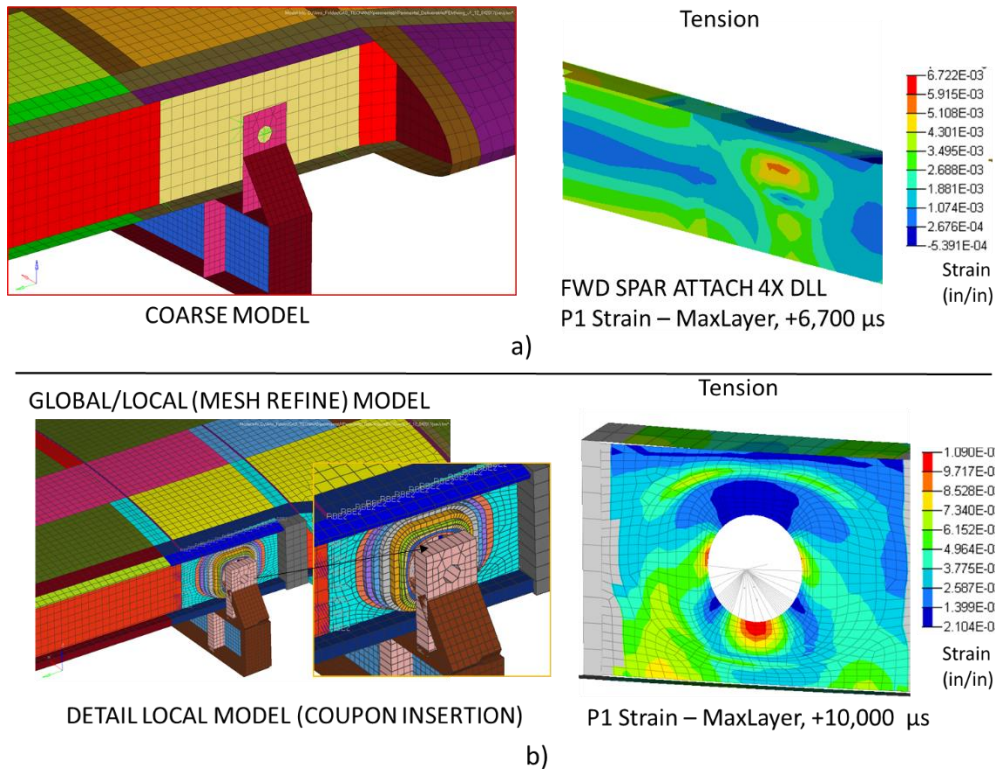


Figure 17: a) Global coarse sizing FEM with strain performance (right), b) Local modeling of ply-based coupon insertion to global wing model with strain performance (right)

The global-local FEM, using a ply-based coupon assembly model within the wing assembly FEM, was used to demonstrate performance differences when compared with the coupon only results in Figure 15. When ultimate loads are applied to this global-local model assembly, out-of-plane displacements were dramatically reduced from over 0.5 inch in the unconstrained coupon to less than 0.11 inch. This was due to a reduction in eccentricity-induced loads created from a lack of mid-span constraints. The global-local model in contrast reveals localized P1 (principle axis) stress concentrations along and perpendicular to the loading axis as shown in Figure 17b. This is in contrast with the results of the coarse model shown in Figure 17a, which shows a lower strain amplitude and broadly distributed strain map which is less conservative. The “local” mesh-refined analysis at the wing attachment location showed up to a 60 percent increase in localized strain concentration compared with the coarse model. Coarse model strains of 6,700 µs increased to over 10,900 µs in the local mesh-refined model utilizing a ply-based representation. The global-local and mid-span constrained models of the coupon possessed a full sine-wave displacement shape with lower amplitude compared with the unconstrained coupon FEM used in the test condition. This was due to a more geometrically constrained structure of the global-local model in Figure 16b which contained adjacent spar caps, not found in the test coupon, that added physical constraints and reduced stresses. This result was also similar to the mid-span constraints placed on the coupon-only FEM of Figure 16b.

To summarize, test results in Figure 13 showed a predominately linear displacement with load from the coupon FEM up to ultimate loading. Matrix cracking resulted in hysteresis (and lower loads with displacement) when returning to the zero load condition, however. The local model analysis for flight-loads remained within material margins at all times, however this was due to high factors of safety used for sizing.¹⁵ The higher stresses encountered with the global-local model demonstrated the importance of representing critical attachment features. These attachment features contained stress concentrations, discovered by locally mesh-refining a coarse sizing model with a full-scale ply-based formulation.

V. Concluding Remarks

A performance-based design method using ply-based modeling was implemented to validate proof-test results for the X-57 aircraft forward wing bearing assembly. The ply-based modeling method was found adequate for detail feature analysis and flight structures validation. As a result of this effort, ply-based modeling techniques will be broadly applied to a future flight-wing assembly proof-test required for airworthiness approval. A full-scale analysis validation approach of wing attachment hardware using ply-based modeling was selected after investigation of a scaled composite test section designed to optimize stress-ratios of spar features. The study used FEM-based parameters of ply thickness and geometric scaling (morphing) to optimize a test-section but highlighted the difficulty of scaling due to reductions in stability and load path variation. The scaled test-section optimization varied ply thickness, spar height, spar cap, and shear-web thickness simultaneously. This approach resulted in quasi-fully stressed design candidates for main spar test section candidates, but with reduced buckling resistance. Spar scaling, however, provided design guidance for evaluation of the main spar and a full-scale bearing test coupon. The ply-based approach modelled the forward spar shear-web more accurately to represent detail features like corner radii and joggles that were obscured during scaling of the standard non ply-based model. Success with ply-based modeling led to use of a full-scale shear-web coupon assembly and ply-based FEM, to implement a quasi-building block approach for the performance-based validation concept. Building block inputs were obtained by comparing standard tensile testing results with the ply-based modeling predictions of a coupon-only FEM, representing the forward spar shear web region. The ply-based coupon analysis did not initially contain mid-span constraints which resulted in high mid-span displacements and over-conservative stress predictions for flight-hardware. This ply-based coupon analysis method, with simulated flight-hardware boundary constraints, however, provided verification of forward spar bearing strength and wing assembly proof-load test performance predictions.

Therefore, ply-based modeling of the full-scale wing spar and shear-web bearing locations was selected to evaluate the effect of more detailed geometric features for the loading of the wing spar critical structures. Stress sizing results of traditional FEMs without mid-span constraints did not fully reflect localized stress behavior or flight-structures performance of critical spar elements. The use of ply-based spar models with adjacent structures like spar caps reduced analysis uncertainty. A shear-web bearing coupon tested to ultimate loads was compared successfully with a full-scale ply-based FEM for displacement and peeling failure mode predictions. The forward spar wing attachment shear-web coupon, with unidirectional fiber dominated inner plies, was inserted into the global flight-wing coarse sizing FEM to capture stress concentrations from the global loads. The shear web coupon stress predictions of this configuration matched the locations of the observed peeling failure and matrix cracking. For all cases examined where the test coupon FEM was analyzed by similarity in loading and boundary constraint, the strain performance remained within material limitations. This methodology provided a performance-based airworthiness compliance element for the X-57 wing structures certification effort on critical structure locations like the main spars.

The full-scale ply-based FEM studies used for test and FEM validation demonstrate the importance of the global-local analysis and boundary constraint representation for critical wing structure attachment locations. Although the wing assembly coarse FEM adequately sizes the structure for vehicle maneuver loads, the local attachment and detail features typically endure significantly higher strain concentrations and requires mesh-refinement analysis at full-scale to guarantee safety margins. Implementation of a full-scale ply-based spar FEM with detail features was used to validate strength margins, and verify peeling failure and matrix cracking locations encountered during test. This method was determined by the flight safety review board to satisfy a building-block requirement for a performance-based certification strategy. Results of this study will be compared with a future flight hardware proof load test for the X-57 wing structure assembly to correlate critical structures with full-scale, ply-based FEM models that support the flight test campaign.

Acknowledgements

This work was funded by the Transformative Aeronautics Concepts (TAC) program for Aeronautic Research Mission Directorate at NASA. The collaboration provided by Xperimental Inc, San Luis Obispo CA and the NASA-AFRC Structures branch in fabricating test coupon hardware and providing bearing coupon test data respectively, is greatly appreciated.

References

- ¹ Stoll, A., Bevirty, J., Moore, M., and Fredericks, W., “Drag Reduction through Distributed Electric Propulsion,” Aviation Technology, Integration, and Operations Conference, June 16-20, 2014, Atlanta, Georgia.
- ² Anon., Title 14 Code of Federal Regulation, Part 23, “Airworthiness Standards: Transport Category Airplanes,” Subpart C “Structure,” Electronic Code of Federal Regulations, http://www.faa.gov/regulations_policies/faa_regulations/, Washington, DC, 2016.
- ³ Moore, J., Cutright, S., “Structural Design Exploration of an Electric Powered Multi-Propulsor Wing Configuration,” AIAA SciTech Conference, Grapevine, Texas, January 13-17, 2017.
- ⁴ http://www.faa.gov/regulations_policies/advisory_circulars/index.cfm/go/document.information/documentID/22660, Washington, DC, July 23, 1998.
- ⁵ Anon., “Composite Materials Handbook Volume 3,” SAE International, *Polymer Matrix Composites Materials Properties*, <https://global.ihs.com/>, March, 2012.
- ⁶ “NASTRAN,” MSC Software, Newport Beach, California, www.mssoftware.com, 2018.
- ⁷ “HyperWorks,” Altair Engineering, Troy, Michigan, www.altair.com, 2015.
- ⁸ Niu, M., “Airframe Structural Design,” Hong Kong Conmilit Press, Hong Kong, 1988.
- ⁹ Simites, G. J., and Rezaeepazhand, J., “Structural Similitude for Laminated Structures,” *Journal of Composites Engineering*, Vol. 3, 1993, pp. 751-765.
- ¹⁰ Simites, G. J., and Rezaeepazhand, J., “Structural Similitude and Scaling Laws for Buckling of Cross-Ply Laminated Plates,” *Journal of ThermoPlastic Composite Materials*, Vol. 8, 1995, pp. 240-245
- ¹¹ Hilburger, M. W, Rose C. A., and Starnes, J.H., “Nonlinear Analysis and Scaling Laws for Noncircular Composites Structures Subjected to Combined Loads,” AIAA Paper 2001-1335, 2001.
- ¹² Anon., “Aircraft Structural Safety of Flight Guidelines,” AFRC G7123.1, Armstrong Flight Research Center Edwards AFB, California, 2014.
- ¹³ Xperimental, LLC , “SCEPTOR Phase III Loads Report”, Report 161210-02A, December 2016.
- ¹⁴ Haftka, R.T., and Gurdal, Z., “*Elements of Structural Optimization*,” Springer Science+Business Media, Dordrecht, Netherlands, 1992.
- ¹⁵ Xperimental, LLC , “SCEPTOR Phase III Stress Report”, Report 161210-02A, December 2016.
- ¹⁶ Jegley, D. C., Przekop, A., Rouse, M., Lovejoy, A. E., Velicki, A., Linton, K., Wu, H. T., Baraja, J., Thrash, P. J., and Hoffman, K., “Development of Stitched Composite Structure for Advanced Aircraft,” Proceedings of the American Society for Composites 30th Technical Conference, Paper 1840, East Lansing, MI, September 2015.
- ¹⁷ Anon., “Standard Test Method for Tensile Properties of Polymer Matrix Composite Materials,” ASTM International, <https://global.ihs.com/>, October, 2017.